

Article

Highly Efficient Hierarchical Porous Carbon Supported Pd-Based Catalysts for Additive-Free Dehydrogenation of Formic Acid

Xinyi Miao¹, Fengwu Tian¹, Miaomiao Bai¹, Yujia Zhang¹, Wei Wang¹ , Zuoping Zhao^{1,2}, Xianzhao Shao^{1,*} and Xiaohui Ji¹

¹ Shaanxi Key Laboratory of Catalysis, School of Chemistry and Environment Science, Shaanxi University of Technology, Hanzhong 723001, China; miaoxinyi000@126.com (X.M.); tianfengwu000@126.com (F.T.); baimiaomiao000@126.com (M.B.); zhangyujia000@126.com (Y.Z.); wangwei@snut.edu.cn (W.W.); zhaozuoping@126.com (Z.Z.); slgjxh@163.com (X.J.)

² State Key Laboratory of Qinba Bio-Resource and Ecological Environment, Shaanxi University of Technology, Hanzhong 723001, China

* Correspondence: xianzhaoshao@snut.edu.cn; Tel.: +86-916-2641660

Abstract: Formic acid (FA) is one of the most prospective hydrogen carriers for renewable energy transformation. In this context, the addition of extra-amine is always required for promoting the reactivity of FA, which is still a key challenge. Herein, we report a simple but effective strategy to synthesize Pd nanoparticles, supported on NH₂-functionalized, phosphorous-doped glucose-based porous carbon (NH₂-P-GC). The introduction of NH₂- groups on the support acts as an immobilized amine-additive for FA dehydrogenation, while phosphorus not only serves as an electronic promoter to keep Pd in the electronic deficient state for FA dehydrogenation, but also as an enlarger of the aperture size of the carbon. As a result, the Pd/NH₂-P-GC has exceptional catalytic activity, 100% H₂ selectivity, CO generation that is undetectable, and good reusability for hydrogen production from FA. In the additive-free dehydrogenation of aqueous FA solution, the initial turnover frequency (TOF) can reach 5126 h⁻¹ at room temperature, which is substantially higher than the best heterogeneous catalyst so far recorded. Overall, the system's high activity, selectivity, stability, and simplicity in producing CO-free H₂/CO₂ gas from FA, without the need for any additive, makes it attractive for practical deployment.

Keywords: formic acid; dehydrogenation; amine functionalization; porous carbon; palladium nanoparticles



Citation: Miao, X.; Tian, F.; Bai, M.; Zhang, Y.; Wang, W.; Zhao, Z.; Shao, X.; Ji, X. Highly Efficient Hierarchical Porous Carbon Supported Pd-Based Catalysts for Additive-Free Dehydrogenation of Formic Acid. *Catalysts* **2022**, *12*, 240. <https://doi.org/10.3390/catal12020240>

Academic Editors: Vincenzo Vaiano and Olga Sacco

Received: 1 February 2022

Accepted: 17 February 2022

Published: 20 February 2022

Publisher's Note: MDPI stays neutral with regard to jurisdictional claims in published maps and institutional affiliations.



Copyright: © 2022 by the authors. Licensee MDPI, Basel, Switzerland. This article is an open access article distributed under the terms and conditions of the Creative Commons Attribution (CC BY) license (<https://creativecommons.org/licenses/by/4.0/>).

1. Introduction

Increased CO₂ emissions due to the ever-increasing consumption of fossil fuels have led to global warming, affecting human beings with serious consequences [1–3]. In view of this, replacing fossil fuels with sustainable energy sources is a prerequisite [4]. Hydrogen is considered to be a future promising source of sustainable energy [5,6]. However, efficient hydrogen storage is a challenge, as a result of low critical temperature and a small value of volumetric energy density [7]. In this regard, chemical hydrogen storage has been widely studied [8,9]. As one of the most prospective hydrogen carriers, formic acid (FA) has a high energy density (53 g L⁻¹, 1.77 kW L⁻¹) [10,11], is non-toxic, and is convenient to use [12–14]. The decomposition of formic acid catalytically leads to the generation of H₂ and CO₂, due to the favorable thermodynamic behavior ($\Delta G^0 = -32.8 \text{ kJ mol}^{-1}$) [15]. However, the catalysts are poisoned due to the formation of CO and H₂O, via undesirable dehydration and decarbonylation pathways [16]. It is imperative to find suitable catalysts with high activity under a mild condition, for selective dehydrogenation of FA, to produce ultrapure H₂ for subsequent utilization in the fuel cells.

Homogenous catalysts are widely investigated for dehydrogenation of FA [17–21], and it has been found that the addition of additives, such as alkali metal formate and triethylamine [22–24], has a great impact on enhancing their catalytic performances. However, additives have been found to have a negative impact on the gravimetric and volumetric H₂ densities, as well as the overall system's energy density. Many metal nanoparticles (NPs) have been reported as heterogeneous catalysts, bringing about the dehydrogenation of FA and they have the advantages of facile fabrication and outstanding reusability [25,26]. Among the reported heterogeneous catalysts, Pd-based catalysts have shown the most encouraging results [27–32]; however, the heterogeneous catalysts have much lower activity compared to the homogeneous counterparts. Compared with the large numbers of FA dehydrogenation systems in the presence of additives, additive free dehydrogenation of FA has been reported scarcely [33]. For the additive-free dehydrogenation of formic acid in the presence of a newly synthesized PdAu-MnO_x/N-SiO₂ catalyst, Karatas et al. obtained an initial turnover frequency (TOF) value of 785 h⁻¹ at room temperature [34]. Yan et al. used NiPd/NH₂-N-rGO as the catalyst for the additive-free dehydrogenation of FA and got an RT TOF value of 953 h⁻¹ [35]. Using freshly synthesized uniform electron-deficient Pd clusters, supported on bi-amino group functionalized SiO₂@graphene oxide, Lu and co-workers obtained a TOF value of 1588 h⁻¹ for additive-free dehydrogenation of FA at 298 K in 2019 [36]. Although attempts have been made to achieve the additive-free dehydrogenation of FA by using the strategy of using amino-group functionalized catalysts, but unsatisfactory catalytic activity is observed, especially at low temperatures. Therefore, development of facile and effective catalysts for ultrapure additive-free H₂ production by dehydrogenation of FA is most sought after.

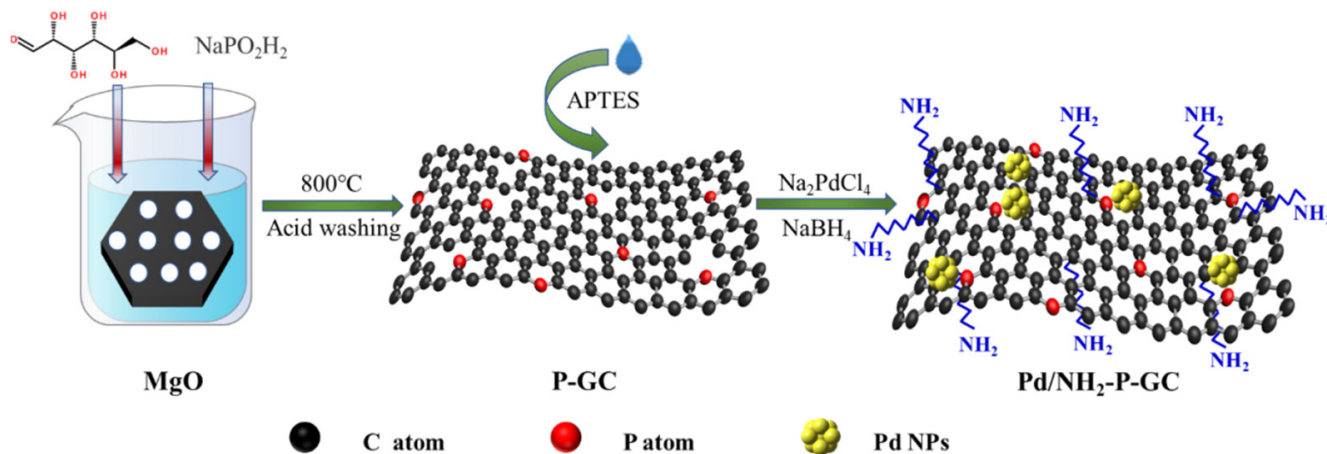
Herein, we prepare supported, well-dispersed Pd NPs, using NH₂-functionalized and P-doped hierarchical porous carbon as the support, by employing an effective and facile method to use it as an additive free catalyst for dehydrogenation of an aqueous FA solution. The P-doped porous carbons were produced by utilizing glucose as the carbon source, MgO as template, sodium hypophosphite as the source of phosphorous by pyrolysis in nitrogen atmosphere, and subsequent washing with dilute HCl. Then the as-prepared P-GC was modified by (3-aminopropyl) triethoxysilane (APTES) to obtain NH₂-P-GC. Further, Pd²⁺ can be deposited on NH₂-P-GC, using NaBH₄ as a strong reducing agent, to obtain uniform Pd NP catalysts. The as-prepared Pd/NH₂-P-GC catalyst obtained 100% selectivity for H₂, as well as high catalytic activity (up to 5126 mol_{H₂} mol_{Pd}⁻¹ h⁻¹), under ambient temperature for dehydrogenation of FA that is completely additive-free, and the obtained activity is even higher than the best reported catalyst so far.

2. Results and Discussion

2.1. Preparation and Characterization of Catalysts

Scheme 1 shows the synthesis procedure of P-GC. An aqueous solution, containing MgO and sodium hypophosphite, is heated at a relatively low temperature (120 °C) in the presence of glucose as a carbon source, to obtain a uniform distribution of MgO and sodium hypophosphite in the precursor structure. Thereafter, thermal annealing of the obtained powder was carried out in a nitrogen atmosphere. During this step, a mesoporous template is formed via high temperature embedding of magnesium oxide in the carbon framework. Simultaneously, a large volume of gases, such as PH₃ and CO₂, will be released continuously, due to the reaction of the negative ions containing phosphorus during the heating process. This will result in the formation of macropores on the intermediate product due to uniform exfoliation by the gases. At the same time, the gases will be effectively inserted into the carbon lattice by overcoming the van der Waals attraction between the carbon layers, leading to the doping of the elements O and P, partially into the carbon matrix. Decomposition of glucose during the process of carbonization and the activation of gas may cause micropores. Finally, removal of magnesium oxide nanoparticles via washing of the intermediate product with the HCl leads to the formation of mesopores. After grafting 3-aminopropyltriethoxysilane (APTES) to P-GC, then obtained NH₂-functional

black powder P-GC was employed as a carrier to fix Pd NPs. The obtained Pd/NH₂-P-GC after centrifugation and washing was subsequently characterized and applied for the catalytic dehydrogenation reaction. Supplementary Table S1 gives the ICP determined Pd content of the catalyst along with the results from the XPS investigation.



Scheme 1. Schematic illustration of the synthesis of the P-GC support and Pd/NH₂-P-GC catalyst.

The transmission electron microscope (TEM) image of the parent NH₂-P-GC, as shown in Figure 1, clearly detected wrinkled carbon nanosheets. The carrier exhibits a layered state, which has a rough surface. High-resolution transmission electron microscopy (HRTEM) was conducted to characterize the morphology and microstructure of the typical Pd/NH₂-P-GC specimen. The TEM image indicated rich porous channels of the catalyst and evenly dispersed distribution of the Pd nanoparticles in all the synthesized catalysts, owing to the large surface area of the carbon support derived from biomass. The sizes of the Pd nanoparticles were found to be substantially influenced by phosphorus incorporation in the carbon support. Relatively wide distribution was observed for the size of Pd/NH₂-GC nanocatalysts, with an average size of 2.54 nm (Supplementary Figure S1). But for the Pd/NH₂-P-GC, prepared under identical experimental conditions (i.e., impregnation followed by NaBH₄ reduction), narrower size distribution was observed, with a smaller mean nanoparticle size of 1.47 nm. These results confirm that the P atoms serve as the anchoring sites to the metal precursor, leading to well-distributed Pd nanoparticles with a smaller size. Supplementary Figure S2 is the inverse FFT (IFFT) of the selected area of the HRTEM photograph, showing typical lattice fringes and indicating 0.229 nm as the distance between the crystal planes corresponding to the distance between the Pd {111} planes [37]. The EDS spectra, along with EDS elemental mappings, confirm the co-existence of N, Pd and P elements, which are uniformly dispersed. This proves that the carrier was successfully doped with P atoms and APTES was hydrolyzed and grafted with -NH₂.

The porosities of different materials were examined by N₂ physisorption at 77 K. The isotherms are presented in Figure 2a. The existence of micropores in all the materials is shown in the adsorption isotherm of N₂ (strong adsorption at relatively low pressures, close to zero), with adsorption in the P/P_0 range of ~0.1–0.8, suggesting the existence of small mesopores in all the materials. Thus, it can be verified that the as-synthesized materials exhibit a hierarchical micro-/mesoporous structure. The pore size distribution, depicted in Figure 2b, shows the presence of micro and small mesopores. A similar size range of ~1.2–1.3 nm for all the materials is seen for the micropore system, except for the Pd/NH₂-GC. Meanwhile, the size of the mesopore system is centered at ~3.5 nm in the case of GC and P-GC, which is enlarged to around 4–5 nm after the incorporation of Pd NPs. Table 1 shows the various structural parameters of different materials. The calculated surface areas of GC, P-GC, Pd/NH₂-GC, and Pd/NH₂-P-GC, based on the BET method, were 1070, 1191, 482, and 495 m²g⁻¹, respectively. The significantly decreased specific surface area, pore size, and pore volume of Pd/NH₂-P-GC, and other catalysts,

in comparison to P-GC and GC revealed successful modification of the surface of P-GC by the amine group, and the evenly distributed small Pd NPs occupy the mesopores of NH₂-P-GC. Furthermore, it is evident that the addition of NaH₂PO₂ in the precursor results in an increasing population of the mesopores in the synthesized carbons, as demonstrated by the decreased V_{mic}/V_{total} ratio. The existence of a hierarchically porous structure is conducive to mass transfer. Crystallographic structures of the as-prepared samples were analyzed by XRD (Figure 2c). The amorphous nature of the carbon is indicated by the diffraction peaks at 24.7, 43.1 and 79.8 °C, corresponding to the (002), (100) and (110) planes, respectively [38]. The existence of typically broad absorption peaks at 20–30 °C, in all the materials corresponding to the amorphous carbon, which can be ascribed to the graphitic (002) plane, revealed that the framework integrity was maintained in the course of the catalyst synthesis. The peak at around 43 °C corresponds to the graphite (100) plane. For both the Pd/NH₂-P-GC and Pd/NH₂-GC, the absence of Pd diffraction peaks in the wide-angle XRD pattern can be indexed to low metal loading and the well-dispersed nature of the Pd nanoparticles. Figure 2d shows the FT-IR spectra of P-GC, NH₂-P-GC and Pd/NH₂-P-GC. Before functionalization, the mesoporous carbon support P-GC showed bands at 1576 and 2926 cm⁻¹ [39], corresponding to the C–C and C–H vibrations of the graphite domain. The band observed at 3432 cm⁻¹ can be indexed to the surrounding atmospheric moisture bound to the carbon surface [39]. However, after amination, bands at 754, 1020, and 3578 cm⁻¹ appeared, which may be ascribed to the out-of-plane bending, C–N stretching and N–H plane of the –NH₂ group, respectively [40]. The shoulder at 3578 cm⁻¹ arises from the N–H extension frequency of the –NH₂ group [41]. Two more bands at 894 and 1621 cm⁻¹, corresponding to the out-of-plane and in-plane N–H bending vibrations [35], respectively, confirmed the presence of amine groups (NH₂-) on the P-GC.

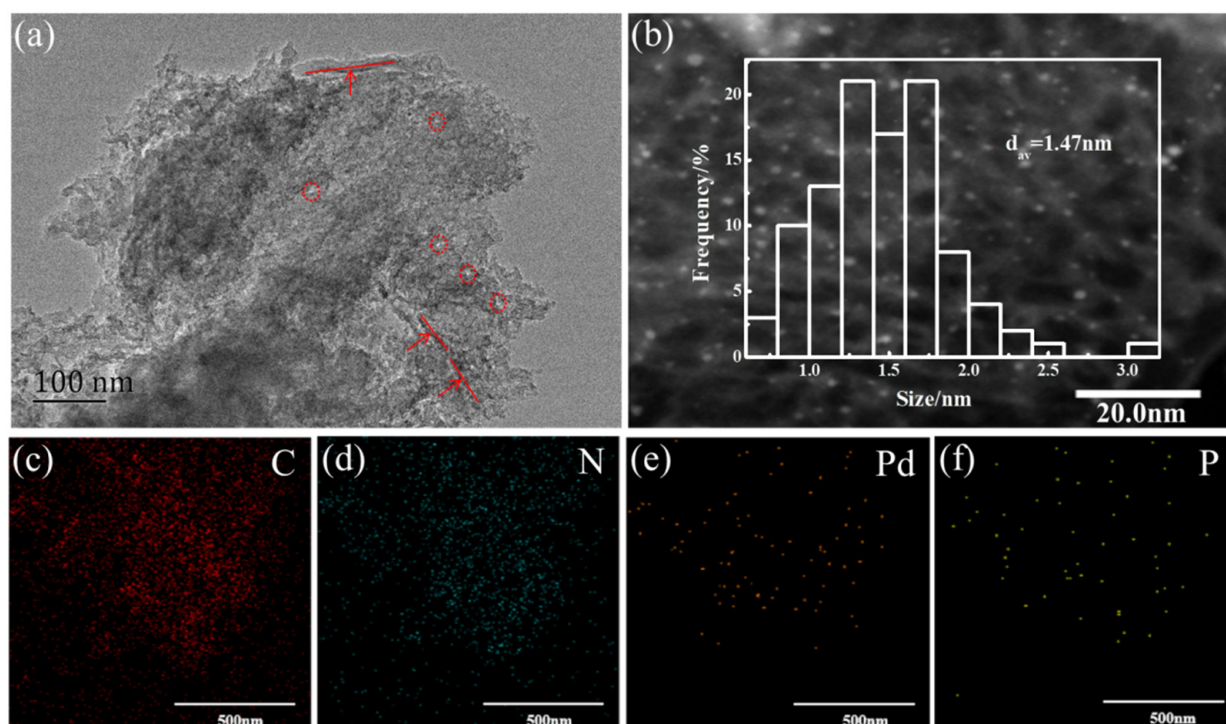


Figure 1. (a) TEM image of NH₂-P-GC, (b) HRTEM image and histograms with Pd nanoparticle size distributions of Pd/NH₂-P-GC, (c–f) EDS elemental mappings of Pd/NH₂-P-GC.

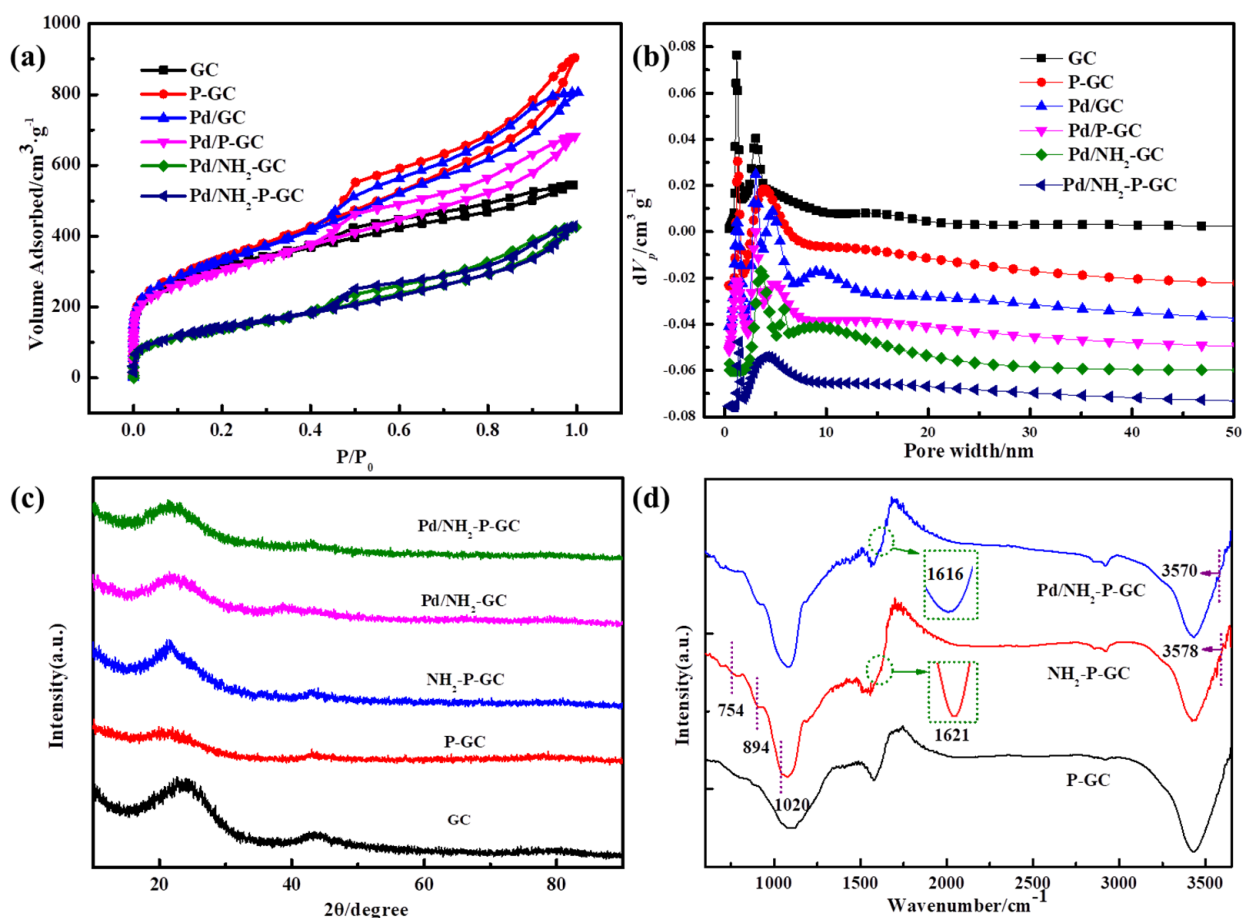


Figure 2. (a) Nitrogen adsorption–desorption isotherms and (b) corresponding pore size distribution curves of GC, P-GC, Pd/GC, Pd/P-GC, Pd/NH₂-GC and Pd/NH₂-P-GC. (c) XRD patterns of GC, P-GC, NH₂-P-GC, Pd/NH₂-GC and Pd/NH₂-P-GC. (d) FT-IR spectra of P-GC, NH₂-P-GC and Pd/NH₂-P-GC.

Table 1. Textural characteristics of various samples.

Sample	S _{BET} ^a (m ² g ^{−1})	V ₀ ^b (cm ³ g ^{−1})	V _t ^c (cm ³ g ^{−1})	D _{pore} ^d (<2 nm)	D _{pore} (>2 nm)
GC	1070	0.84	0.65	1.2	3.2
P-GC	1191	1.37	0.74	1.3	3.8
Pd/GC	1143	1.23	0.76	1.2	3.2, 4.6, 9.1
Pd/P-GC	1055	1.04	0.64	1.2	3.2, 4.9
Pd/NH ₂ -GC	482	0.65	0.33	-	3.5, 5.8
Pd/NH ₂ -P-GC	495	0.66	0.31	1.3	4.1

^a Surface area was calculated using the BET method at $P/P_0 = 0.05–0.3$. ^b Total pore volume at $P/P_0 = 0.99$. ^c Evaluated by the t-plot method. ^d Pore diameters at the maximum of pore size distribution determined by the NLDFT method.

2.2. Catalytic Performance for FA Dehydrogenation

Selective decomposition of FA, in the presence of Pd/NH₂-P-GC, as well as other materials as a catalyst, has been compared in Figure 3a. In the presence of Pd/NH₂-P-GC as catalyst, 244 mL of gases are released within 13 min, as evident in Figure 3a, representing H₂ selectivity of 100% and an initial TOF value of 5126 h^{−1}. Also important to note, the gas mixture for the catalyst of Pd/NH₂-P-GC comprised H₂ and CO₂, in the volume ratio of 1:1, but no carbon monoxide (CO) could be detected using gas chromatography (GC) (Supplementary Figure S3) and NaOH trapping (Supplementary Figure S4). As compared, in the absence of P in the Pd NPs, the obtained catalyst Pd/NH₂-GC showed inferior catalytic activity (244 mL of gas released at a reaction time of 26 min). None of the catalysts, Pd/NH₂-P-GC and Pd/NH₂-GC, required a base as additive to realize the

FA dehydrogenation reaction. The initial turnover frequency (5126 h^{-1}) of Pd/NH₂-P-GC for the dehydrogenation of formic acid is found to be the highest among all the additive-free heterogeneous catalysts, reported in the literature (Supplementary Table S2), and encouragingly, this value can even be compared with those of in the presence of additives or/and at elevated temperature. However, the Pd/GC and Pd/P-GC are found to be nearly inactive for the dehydrogenation reaction of FA. It can be ascribed to the Brønsted basic sites of amino groups on GC, which act as proton scavengers for formic acid by complexing with the proton of the formic acid molecule to promote the activity of dehydrogenation of FA. The existence of amino groups upon the surface of the catalyst, on the other hand, will facilitate electron transport from the host to the Pd NPS, resulting in an electron-rich surface and better catalytic efficiency for hydrogen production from FA [35,37,41]. As shown in Figure 3c, the number of APTES (amine group) grafted on P-GC has a notable impact on the catalytic activity of Pd/NH₂-P-GC. Both small and large quantities of APTES showed negative impact on the catalytic performance. If the APTES amount is lesser, the effective stabilization of metal nanoparticles is not possible, leading to larger and coalescent particles. However, if an excess amount of APTES was added, the active sites were encapsulated and, hence, the reactants could not diffuse to the active sites. Though the surface grafted amino groups (-NH₂) of the carrier serve as the interaction sites for fixing the metal nanoparticles and also prevent the aggregation of nanoparticles into large particles, excess amino groups will block the pores of the carrier, resulting in the hinderance for the diffusion of reactants to the active sites, and thereby reducing the catalytic activity. Therefore, the dosage of APTES was set at 0.3 mL.

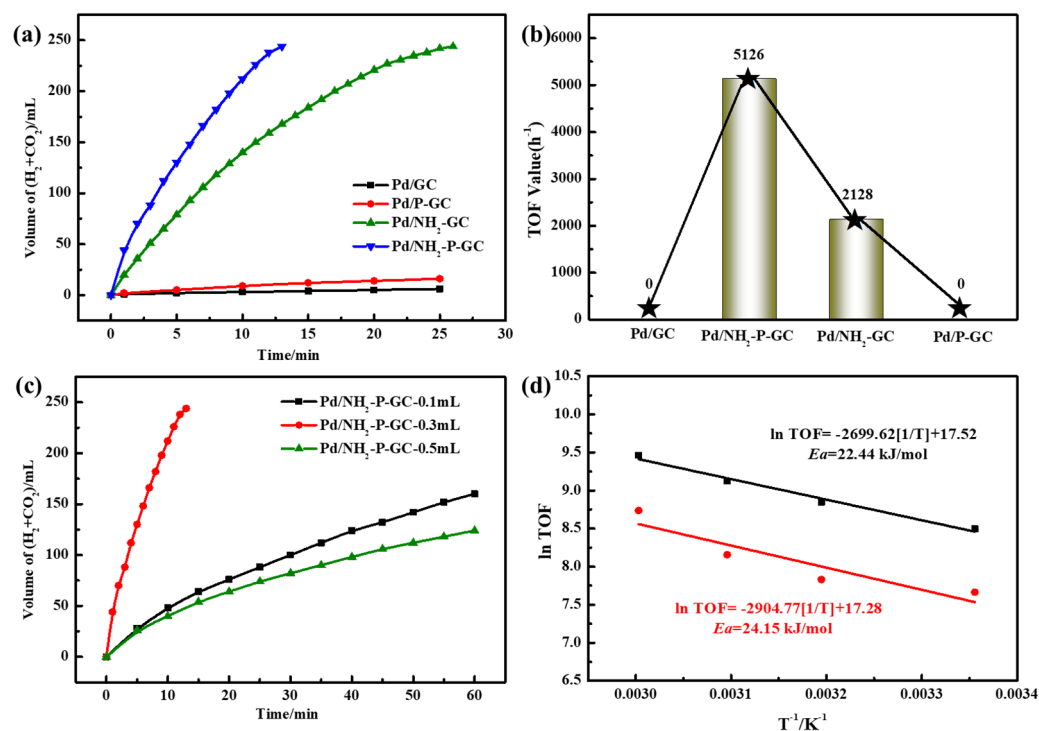


Figure 3. (a) Gaseous generation during the decomposition of FA versus time in the presence of Pd with/without different supports or APTES and (b) the corresponding TOF value (c) comparative gaseous product generation for varying amounts of APTES in Pd/NH₂-P-GC; (d) the calculated activation energy at different sample temperatures. (Black line representative of Pd/NH₂-P-GC sample, red line representative of Pd/NH₂-GC sample) (Reaction conditions: 5 mL 1.0 M FA, $n_{\text{Pd}}/n_{\text{FA}} = 0.0037$).

The kinetics of the FA dehydrogenation were assessed to further examine the unique catalytic behavior of this Pd/NH₂-P-GC catalyst. As shown in Figure 4a, the temperature-dependent catalytic activity of Pd/NH₂-P-GC was investigated by studying the dehydrogenation reaction of FA at different set temperatures (298, 313, 323 and 333 K) and

the corresponding initial TOF values were 5126, 7299, 9577 and 13,479 h^{-1} , respectively. Increasing the temperature provides the required activation energy of the reaction quickly for facilitating the reaction, making apparent activation energy (E_a) a key index for the dehydrogenation system. The apparent activation energy for the dehydrogenation of FA in the presence of Pd/NH₂-P-GC as a catalyst was found to be 22.44 kJ/mol from the plot of $\ln(\text{TOF})$ vs. $1/T$ (Figure 3d), as per the Arrhenius equation, indicating lower activation energy compared to other values reported (Supplementary Table S2) [42–45]. For example, as a catalyst for the dehydrogenation of formic acid, the corresponding calculated activation energy for the Pd, supported on N-doped porous carbon, was found to be 48.8 kJ mol⁻¹ by Chaparro-Garnica et al. [46]. Luo et al., found the activation energy of 30.14 kJ mol⁻¹ for the H₂ production from FA, using dispersed IrPdAu alloy nanoparticles on amine-modified mesoporous SiO₂(NH₂-SBA-15) [47]. In addition, for the Pd/NH₂-GC catalyst, the apparent activation energy of the catalyst was found to be 24.15 kJ/mol, thereby proving that the doping of P in the carrier has an excellent effect on the dehydrogenation of FA. The values of E_a lying in the typical diffusion energy barriers range (20–30 kJ mol⁻¹) suggested that mass transport was the restricting factor for the performance of Pd NPs, supported on mesoporous and microporous materials of this kind and the apparent E_a was indicating the diffusion energy barrier in actuality [48]. Moreover, we have explored in depth the variation of formic acid concentration, as shown in Figure 4c. The results of the correlational analysis are set out in Figure 4c,d, in terms of formic acid concentration, the dehydrogenation reaction appears as a zero-order reaction.

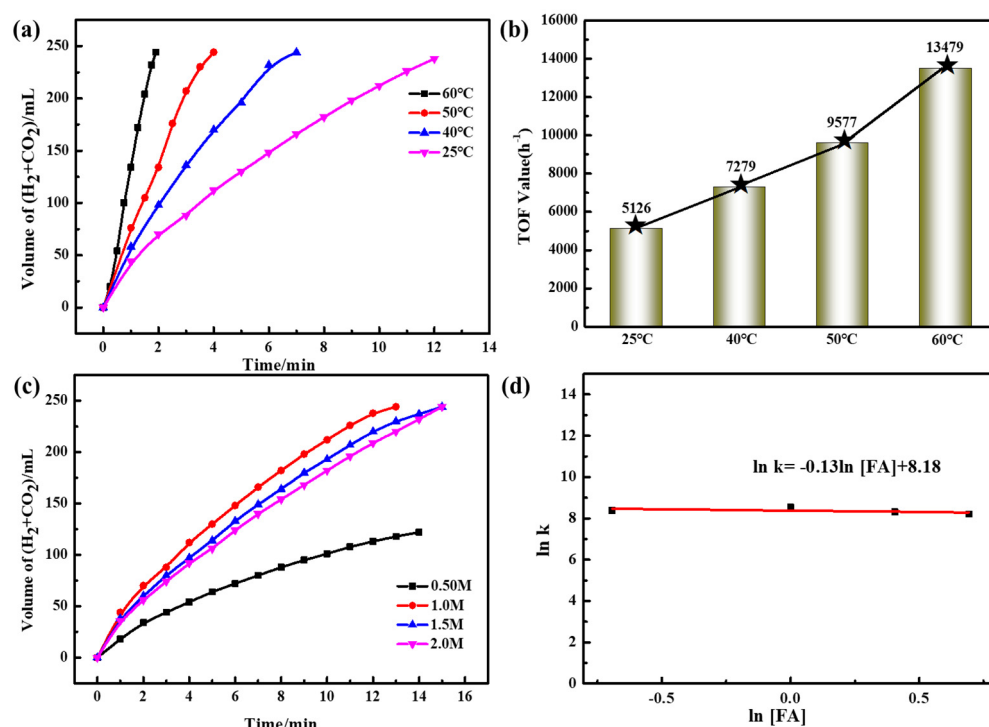


Figure 4. Gaseous generation during the decomposition of FA with respect to time in the presence of Pd/NH₂-P-GC at different (a) reaction temperatures, (b) corresponding initial TOF values, (c) FA concentrations, and (d) reaction kinetics for the concentration variable. (Reaction conditions: $n_{\text{Pd}}/n_{\text{FA}} = 0.0037$).

To further study the chemical valence and electronic states of various elements for different catalysts, X-ray photoelectron spectroscopic (XPS) analysis of all the catalysts was prepared. Supplementary Figure S5 depicts the XPS full spectrum of the Pd/NH₂-P-GC sample, from which the characteristic peaks of C, N, O, P, Si, Pd can be accurately identified. As revealed by the P 2p spectrum (Supplementary Figure S6), the P species present in Pd/NH₂-P-GC are the ones typically found in carbon materials, i.e., P–C

(132.6 eV) and P–O (133.4 eV) [49]. The presence of N 1s peak at about 400.0 eV, attributed to the NH₂ group in Figure 5a [50], which illustrates the successful grafting of amine functional groups on P-GC, and is consistent with the FT-IR spectra (Figure 2d). In order to investigate the electronic states of Pd, XPS analysis was carried out on the catalysts Pd/NH₂-GC, Pd/NH₂-P-GC and Pd/P-GC, the high resolution XPS spectra of Pd 3d for different catalysts could be deconvoluted into two doublets, corresponding to Pd⁰ and Pd²⁺ 3d electron states [51]. As can be seen in Figure 5b, metallic Pd⁰ is the main component of Pd for Pd/P-GC (Pd⁰: 54%, Pd²⁺: 46%) and Pd/NH₂-GC (Pd⁰: 76%, Pd²⁺: 24%). Pd/NH₂-P-GC showed a shift of ~0.2 eV (from 336.4 eV to 336.6 eV) towards higher binding energies in the Pd spectrum, compared to that of Pd/NH₂-GC, which confirmed the modification of the electronic properties of the Pd species by their interaction with the phosphorus functionalities incorporated in the catalysts. Meanwhile, for both the Pd/P-GC and Pd/NH₂-P-GC catalysts, the binding energies of zero-valent Pd 3d for Pd/NH₂-GC (336.2 and 338.0 eV) shifted towards higher values (336.6 and 338.9 eV), confirming that the functionalization of amine groups enhances the strength of the interaction among the carrier and metal, thus, changing the valence electron state of Pd [52–54]. Such a positive shift of Pd spectra suggests the generation of electron-deficient Pd species and is additionally verified by the relative proportion of Pd⁰ and Pd²⁺ (Pd⁰: 47%, Pd²⁺: 53%, Pd⁰/Pd²⁺ almost as 1:1) in Pd/NH₂-P-GC. This is because a part of Pd²⁺ is not reduced due to strong metal–support interactions (SMSI), even when exposed to a strong reducing agent of the type of NaBH₄, such that nitrogen atoms and amine functional groups, incorporated in the support, tend to stabilize the Pd²⁺ species [36]. Therefore, Pd/NH₂-P-GC potentially owes its better catalytic activity to the smaller size and high dispersion of Pd NPs and SMSI by amine groups and the doping of P in the carrier.

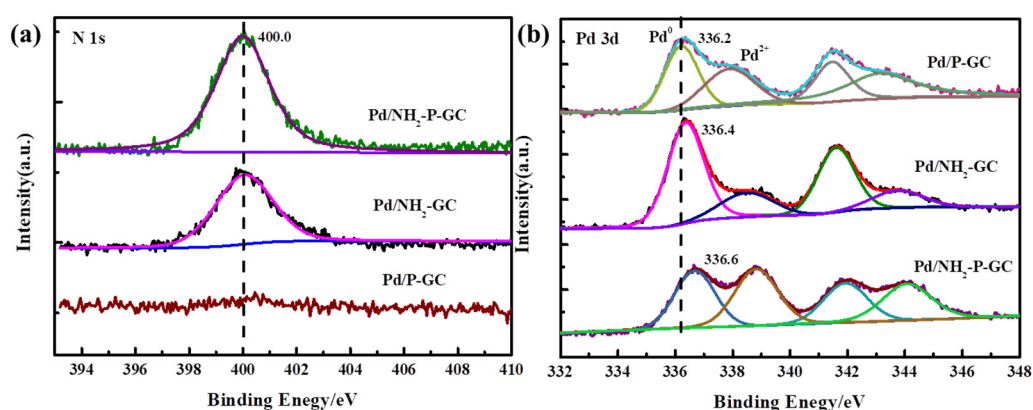


Figure 5. High-resolution XPS spectra of (a) N 1s and (b) Pd 3d in Pd/NH₂-GC, Pd/NH₂-P-GC and used Pd/NH₂-P-GC.

2.3. Catalytic Mechanism and Stability

To prove the mechanism of FA dehydrogenation, we conducted comparative experiments under different conditions. As shown in Figure 6a, the Pd/P-GC catalyst has almost no catalytic activity in the presence of FA or formate. When the ratio of FA to formate is 1:1, Pd/P-GC showed obvious catalytic activity, and the FA decomposition was completed within 26 min, showing that the FA dehydrogenation reaction takes the formate path. Figure 6b depicts a possible chemical route for hydrogen synthesis from FA catalyzed by Pd/NH₂-P-GC, based on the aforementioned findings and prior reports [55–59]. When the FA molecule comes close to the active sites of the Pd NPs, the surrounding amine group affords Brønsted basic sites and acts as a proton scavenger to speed up the deprotonation of the O–H band. The production of the -Pd-HCOO^- complex and the $\text{-[H}_2\text{NH]}^+$ group follows the deprotonation process. The -Pd-HCOO^- complex and $\text{-[H}_2\text{NH]}^+$ group undergo additional dehydrogenation to liberate H₂ and CO₂ via the elimination pathway, thanks to the electron-rich Pd NPs surface. Finally, other FA molecules will be able to access the

electron-rich surface active sites of Pd NPs. As a result, it is plausible to conclude that the surface amine groups on P-GC, as well as the high dispersion of ultrafine and electron-rich Pd NPs, with plentiful and accessible active sites, lead to improved catalytic performance for quick hydrogen production from FA solution.

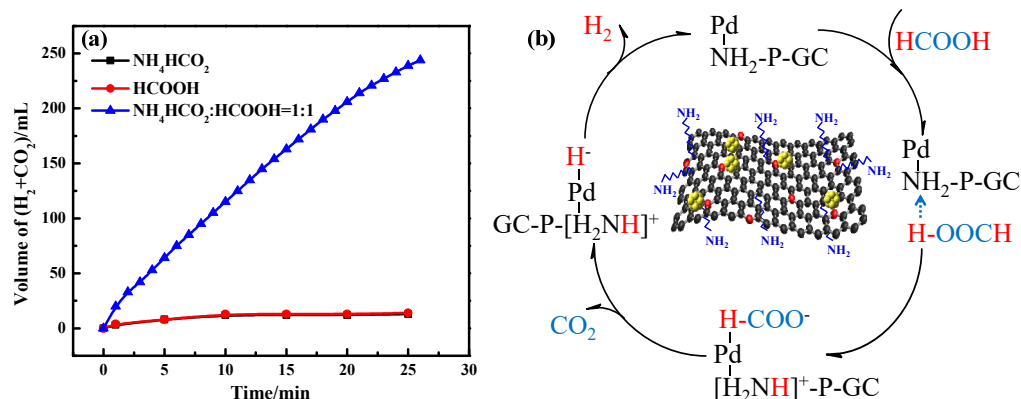


Figure 6. (a) Gaseous generation during the decomposition of different reagents with respect to time in the presence of Pd/P-GC. (b) Schematic illustration of plausible mechanism for the decomposition of FA over Pd/NH₂-P-GC.

Finally, the stability of the Pd/NH₂-P-GC catalyst during FA decomposition was tested. As can be seen in Supplementary Figure S7 (Supplementary Materials), the H₂ generation rate and production remained almost unchanged, even after five cycles, indicating the excellent stability of the Pd/NH₂-P-GC catalyst. Notably, also, Supplementary Figure S1e,f shows that the Pd particle size of the used catalyst increased slightly, from 1.47 nm to 1.86 nm. The decreased contact between the Pd NPs and the grafted functional groups during the processes can explain the small increase in the size of Pd NPs after recycling. Furthermore, it was discovered using XPS analysis that attributed to the small loss of surface amine functional groups, which was supported by the results in Supplementary Table S1. The minor activity attenuation is most likely due to the lowered amine groups and increased catalyst particle size.

3. Materials and Methods

3.1. Chemicals and Characterization Techniques

Formic acid (FA, HCOOH, 96%, Sigma-Aldrich, St. Louis, MA, USA), MgO powder (Sinopharm Chemical Reagent Beijing Co., Ltd, Beijing, China), glucose (C₆H₁₂O₆), sodium hypophosphite (NaH₂PO₂), (3-aminopropyl) triethoxysilane (APTES, C₉H₂₃NO₃Si, 99%, Aladdin Chemistry Co., Ltd., Shanghai, China), palladium (II) chloride (PdCl₂, Pd >59%, Sinopharm Chemical Reagent Co., Ltd., Shanghai, China), sodium chloride (NaCl, >99.5%, Sinopharm Chemical Reagent Co., Ltd.), sodium borohydride (NaBH₄, 96%, Sinopharm Chemical Reagent Co., Ltd.) were used during the experiments. Aqueous solutions were prepared by using de-ionized water having a specific resistance of 18.2 MΩ·cm.

For accurate estimation of Pd content, inductively coupled plasma-atomic emission spectroscopy (ICP-OES, PerkinElmer 8300, PerkinElmer, Waltham, MA, USA) was used to analyze the as-prepared catalysts. The electrical and compositional properties of the surface elements and valence states were examined using an X-ray photoelectron spectrometer (XPS) with a Thermo Fisher ESCALAB 250XI instrument (Thermo Fisher Scientific, PerkinElmer, Waltham, MA, USA) and a K-alpha spectrometer. Hitachi SU8010 and JEOL-JEM-2010 instruments were respectively used to obtain scanning and transmission electron microscopy (SEM and TEM) photographs. The materials' XRD patterns were measured by making use of a Bruker D8 Advance equipment with Cu-Kα radiation (40 kV, 55 mA). Room temperature IR of the specimens was measured by Fourier Transform Infrared spectrometer (Nicolet iS10). An automated gas sorption analyzer (Belsorp Max) was used to obtain the

N₂ adsorption–desorption isotherms of specimens, after degassing the samples at 200 °C for 6 h to measure the surface area of the specimens by employing the Brunauer–Emmert–Teller (BET) technique. Pore size distribution was determined from the Belsorp Max instrument software package employing the nonlocal density functional theory (NLDFT) model. Analysis of the evolved gases during the H₂ generation process was carried out by gas chromatography (Panna A91 Plus) with a Porapak Q column (4.0 m × 2.0 mm) using a TCD detector.

3.2. Preparation of Phosphorus-Doped Porous Carbon

Carbonization at elevated temperature which followed a preliminary heating was used to prepare the phosphorus-doped porous carbons (P-GC). In the first step, a solution of MgO powder in deionized water was prepared by employing a continuous ultrasonic agitation over a period of 1 h and subsequently the mixture was boiled for 24 h under reflux. After that, the mixture was filtered and dried followed by calcination at 550 °C for 1 h for the removal of water subsequently forming porous MgO template [37]. Then, in two different containers, two different dispersions were prepared, in one dispersion of 9.0 g glucose and 10.0 g MgO template in 50 mL deionized water and in the other one dispersion of 1.0 g sodium hypophosphite in another 25 mL deionized water. The latter dispersion was then vigorously agitated into the previous mixture to generate a homogenous solution. The solution was then heated in an oven at 120 °C for 12 h to produce a brown powder. After that, the powder was annealed by heating it in a tube furnace at 800 °C for 1 h under a nitrogen environment at a rate of 5 °C min⁻¹. From the as-obtained intermediate products, removal of MgO template was achieved by washing with 1 M HCl solution. In the final step, overnight drying of the samples took place at 80 °C after filtering the sample and then washing with abundant distilled water. The as-obtained samples were labeled as P-GC. Identical preparation method was followed in the absence of sodium hypophosphite to prepare GC for comparative study.

3.3. Preparation of Pd-Based Catalysts

Initially Na₂PdCl₄ (Pd: 4 wt%) aqueous solution was prepared by solubilizing NaCl (0.44 g) and PdCl₂ (0.66 g) into 8.9 g H₂O under magnetic stirring for 3 h. Typically, Pd/NH₂-P-GC preparation involves the addition of APTES (0.3 mL) into the P-GC aqueous solution (2 mg/mL, 75 mL) and sonicated for 30 min at 298 K. Subsequently, Na₂PdCl₄ (Pd: 4 wt%, 150 mg) was added into the prepared mixture under magnetic stirring for 1 h. Finally, the solution was again magnetically stirred for 1 h to dissolve NaBH₄ (100.0 mM, 125 mg) in the above mixed solution. The resultant black product was separated and washed with water and ethanol several times and was termed as Pd/NH₂-P-GC. We also synthesized Pd supported on GC, Pd/P-GC and Pd/NH₂-GC using the same procedure with/without APTES.

3.4. Catalytic Activities and Recycling Stability for Dehydrogenation of FA

50 mg of the as-prepared Pd/NH₂-P-GC catalyst was placed inside a two-necked round-bottom flask to evaluate its catalytic activity. One neck was attached to a gas burette, while the other was connected to a pressure-equalization funnel for the entry of aqueous formic acid (FA) (1.0 M, 5.0 mL). After adding the FA solution, the catalytic reaction was started with magnetic stirring (600 × g rpm). Monitoring of the evolved gas was done by the gas burette. After the first run of the dehydrogenation reaction was completed, the spent catalyst was separated by centrifugation and washed with water and ethanol, then dried in vacuum at 60 °C. Afterwards, the recovered Pd/NH₂-P-GC catalyst was redispersed, and the dehydrogenation reaction re-started with 5.0 mL FA solution readded into the reaction system and gas evolution was measured in the burette. Similar method was applied to study the catalytic activities of other catalysts for FA decomposition. In all the experiments, molar ratio of metal:FA (n metal/n FA) for all the catalysts was maintained at 0.0037.

Temperature during all the experiments was maintained at 298 K under ambient pressure except for specified. All the experiments were carried out twice with repeatable results.

3.5. Calculation Methods

The turnover frequency (TOF) value was computed on the basis of the total number of Pd atoms supplemented into the reaction system, and is calculated from the following equation:

$$X_{\alpha} = \frac{P_{atm} V_{gas} / RT}{2n_{FA}} \quad (1)$$

$$TOF_{initial} = \frac{P_{atm} V_{gas} / RT}{2n_{metal} t} \quad (2)$$

where X_{α} is the conversion rate; V_{gas} is the volume of the gas ($H_2 + CO_2$) produced by the reaction; P_{atm} is the atmospheric pressure (101,325 Pa); T is the room temperature (298 K); R is the universal gas constant ($8.3145 \text{ m}^3 \cdot \text{Pa} \cdot \text{mol}^{-1} \cdot \text{K}^{-1}$); n_{FA} is the number of moles of formic acid; $TOF_{initial}$ represents the initial conversion frequency (h^{-1}) when X_{α} reaches 20%; n_{metal} represents the moles of metal Pd in the catalyst, and t denotes the reaction time (h) required for X_{α} to reach 20%.

4. Conclusions

In summary, a facile impregnation–reduction strategy has been applied successfully to prepare a Pd/NH₂-P-GC catalyst by using P-GC as the support for the catalytic dehydrogenation of formic acid. The effective synergy between NH₂-P-GC and Pd NPs realized the transformation of Pd NPs from the inactive to the active state for H₂ generation from FA, and the resulting Pd/NH₂-P-GC catalyst exhibited excellent catalytic activity, with a TOF value of up to 5126 mol_{H₂} mol_{Pd}^{−1} h^{−1} and 13,479 mol_{H₂} mol_{Pd}^{−1} h^{−1} at 298 K and 333 K, good stability and 100% H₂ selectivity for additive-free dehydrogenation of FA. As such, the presence of amino functional groups facilitates the anchoring of dispersing NPs on substrate, it facilitates deprotonation of FA. The P doping of the carrier acts as a pore expander, as well as an electron promoter, to modify electronic properties of Pd NPs for the dehydrogenation of formic acid. That electron deficient Pd was the active center in the FA dehydrogenation reaction, proved by detailed XPS analysis. We predict this generalized fabrication method can also be adapted to fabricate uniform and functionalized Pd catalysts for other catalytic applications.

Supplementary Materials: The following are available online at <https://www.mdpi.com/article/10.3390/catal12020240/s1>, Figure S1: HRTEM image and histograms with Pd nanoparticle size distributions of Pd/P-GC (a,b); Pd/NH₂-GC (c,d) and Pd/NH₂-P-GC-Used (e,f), Figure S2: HRTEM image and corresponding FFT pattern of Pd/NH₂-P-GC, Figure S3: GC spectrum using TCD for the evolved gas from FA aqueous solution, Figure S4: Volume of generated gas (H₂ + CO₂) versus time for the dehydrogenation of FA without additive at 298 K over Pd/NH₂-P-GC with/without 10M NaOH trap, Figure S5: XPS survey spectra of Pd/NH₂-P-GC, NH₂-P-GC and P-GC, Figure S6: High-resolution XPS spectra of P 2p in Pd/NH₂-P-GC, Figure S7: Recyclability of Pd/NH₂-P-GC for FA dehydrogenation, Table S1: ICP-OES (Pd) and XPS analyses (P, N, C, and Si) for Pd/NH₂-P-GC before/after dehydrogenation reaction, Table S2: Initial TOF values for the decomposition of FA without additive over various heterogeneous catalysts.

Author Contributions: X.M.: Conceptualization, Methodology, Investigation, Writing—original draft. F.T.: Investigation. M.B.: Investigation. Y.Z.: Investigation. W.W.: BET experiments and analysis. Z.Z.: Funding acquisition, Writing—review and editing. X.S.: Supervision, Funding acquisition, Writing—review and editing. X.J.: Funding acquisition, Writing—review and editing. All authors have read and agreed to the published version of the manuscript.

Funding: This research was funded by the Natural Science Basic Research Program of Shaanxi (S2020-JC-WT-0001), the Key Research and Development Program of Shaanxi (2020ZDLGY11-06), the Scientific Research Plan Projects of Shaanxi Education Department (20JS014) and Scientific Research Project of City-University Co-construction of Shaanxi Province (SXC-2108).

Institutional Review Board Statement: Not applicable.

Informed Consent Statement: Not applicable.

Data Availability Statement: Data are available in the main text.

Conflicts of Interest: The authors declare no conflict of interest.

References

1. Höök, M.; Tang, X. Depletion of Fossil Fuels and Anthropogenic Climate Change—A Review. *Energy Policy* **2013**, *52*, 797–809. [CrossRef]
2. Trends in Atmospheric Carbon Dioxide. Global Monitoring Laboratory. Available online: <http://www.esrl.noaa.gov/gmd/ccgg/trends/> (accessed on 26 April 2020).
3. Butler, C.D. Climate change, health and existential risks to civilization: A comprehensive review (1989–2013). *Int. J. Environ. Res. Public Health* **2018**, *15*, 2266. [CrossRef]
4. Chu, S.; Majumdar, A. Opportunities and challenges for a sustainable energy future. *Nature* **2012**, *488*, 294–303. [CrossRef] [PubMed]
5. Brandon, N.P.; Kurban, Z. Clean energy and the hydrogen economy. *Phil. Trans. R. Soc. A* **2017**, *375*, 20160400. [CrossRef] [PubMed]
6. Bolatkhan, K.; Kossalbayev, B.D.; Zayadan, B.K.; Tomo, T.; Veziroglu, T.N.; Allakhverdiev, S.I. Hydrogen production from phototrophic microorganisms: Reality and perspectives. *Int. J. Hydrog. Energy* **2019**, *44*, 5799e811. [CrossRef]
7. He, T.; Pachfule, P.; Wu, H.; Xu, Q.; Chen, P. Hydrogen carriers. *Nat. Rev. Mater.* **2016**, *1*, 16067–16083. [CrossRef]
8. Preuster, P.; Papp, C.; Wasserscheid, P. Liquid organic hydrogen carriers (LOHCs): Toward a hydrogen-free hydrogen economy. *Acc. Chem. Res.* **2017**, *50*, 74–85. [CrossRef]
9. Niermann, M.; Drünert, S.; Kaltschmitt, M.; Bonhoff, K. Liquid organic hydrogen carriers (LOHCs)—Techno-economic analysis of LOHCs in a defined process chain. *Energy Environ. Sci.* **2019**, *12*, 290–307. [CrossRef]
10. Eppinger, J.; Huang, K.W. Formic acid as a hydrogen energy carrier. *ACS Energy Lett.* **2017**, *2*, 188–195. [CrossRef]
11. Van Putten, R.; Wissink, T.; Swinkels, T.; Pidko, E.A. Fuelling the hydrogen economy: Scale-up of an integrated formic acid-to-power system. *Int. J. Hydrog. Energy* **2019**, *44*, 28533–28541. [CrossRef]
12. Getman, R.B.; Bae, Y.S.; Wilmer, C.E.; Snurr, R.Q. Review and analysis of molecular simulations of methane, hydrogen, and acetylene storage in metal–organic frameworks. *Chem. Rev.* **2012**, *112*, 703–723. [CrossRef] [PubMed]
13. Grasmann, M.; Laurenczy, G. Formic acid as a hydrogen source—recent developments and future trends. *Energy Environ. Sci.* **2012**, *5*, 8171–8181. [CrossRef]
14. Singh, A.K.; Singh, S.; Kumar, A. Hydrogen energy future with formic acid: A renewable chemical hydrogen storage system. *Catal. Sci. Technol.* **2016**, *6*, 12–40. [CrossRef]
15. Ding, T.Y.; Zhao, Z.G.; Ran, M.F.; Yang, Y.Y. Superior activity of Pd nanoparticles confined in carbon nanotubes for hydrogen production from formic acid decomposition at ambient temperature. *J. Colloid Interface Sci.* **2019**, *538*, 474–480. [CrossRef] [PubMed]
16. El-Nagar, G.A.; Dawood, K.M.; El-Deab, M.S.; Al-Andouli, B.E. Efficient direct formic acid fuel cell (DFAFC) anode of nano-sized palladium complex: High durability and activity origin. *Appl. Catal. B Environ.* **2017**, *213*, 118–126. [CrossRef]
17. Mellmann, D.; Sponholz, P.; Junge, H.; Beller, M. Formic acid as a hydrogen storage material—Development of homogeneous catalysts for selective hydrogen release. *Chem. Soc. Rev.* **2016**, *45*, 3954–3988. [CrossRef] [PubMed]
18. Sordakis, K.; Tang, C.; Vogt, L.K.; Junge, H.; Dyson, P.J.; Beller, M.; Laurenczy, G. Homogeneous catalysis for sustainable hydrogen storage in formic acid and alcohols. *Chem. Rev.* **2017**, *118*, 372–433. [CrossRef]
19. Onishi, N.; Iguchi, M.; Yang, X.; Kanega, R.; Kawanami, H.; Xu, Q.; Himeda, Y. Development of effective catalysts for hydrogen storage technology using formic acid. *Adv. Energy Mater.* **2019**, *9*, 1801275. [CrossRef]
20. Guan, C.; Pan, Y.; Zhang, T.; Ajitha, M.J.; Huang, K.W. An update on formic acid dehydrogenation by homogeneous catalysis. *Chem. Asian J.* **2020**, *15*, 937–946. [CrossRef] [PubMed]
21. Zell, T.; Langer, R. CO₂-based hydrogen storage—Formic acid dehydrogenation. *Phys. Sci. Rev.* **2018**, *3*, 20170012.
22. Jiang, K.; Xu, K.; Zou, S.; Cai, W.B. B-Doped Pd catalyst: Boosting room-temperature hydrogen production from formic acid–formate solutions. *J. Am. Chem. Soc.* **2014**, *136*, 4861–4864. [CrossRef]
23. Wang, N.; Sun, Q.; Bai, R.; Li, X.; Guo, G.; Yu, J. In situ confinement of ultrasmall Pd clusters within nanosized silicalite-1 zeolite for highly efficient catalysis of hydrogen generation. *J. Am. Chem. Soc.* **2016**, *138*, 7484–7487. [CrossRef]
24. Bi, Q.Y.; Du, X.L.; Liu, Y.M.; Cao, Y.; He, H.Y.; Fan, K.N. Efficient subnanometric gold-catalyzed hydrogen generation via formic acid decomposition under ambient conditions. *J. Am. Chem. Soc.* **2012**, *134*, 8926–8933. [CrossRef]
25. Zhong, H.; Iguchi, M.; Chatterjee, M.; Himeda, Y.; Xu, Q.; Kawanami, H. Formic acid-based liquid organic hydrogen carrier system with heterogeneous catalysts. *Adv. Sustain. Syst.* **2018**, *2*, 1700161. [CrossRef]
26. Zhang, L.; Wu, W.; Jiang, Z.; Fang, T. A review on liquid-phase heterogeneous dehydrogenation of formic acid: Recent advances and perspectives. *Chem. Pap.* **2018**, *72*, 2121–2135. [CrossRef]

27. Bulushev, D.A.; Bulusheva, L.G.; Beloshapkin, S.; O'Connor, T.; Okotrub, A.V.; Ryan, K.M. Pd clusters supported on amorphous, low-porosity carbon spheres for hydrogen production from formic acid. *ACS Appl. Mater. Interfaces* **2015**, *7*, 8719–8726. [[CrossRef](#)]
28. García-Aguilar, J.; Navlani-García, M.; Berenguer-Murcia, Á.; Mori, K.; Kuwahara, Y.; Yamashita, H.; Cazorla-Amorós, D. Evolution of the PVP-Pd surface interaction in nanoparticles through the case study of formic acid decomposition. *Langmuir* **2016**, *32*, 12110–12118. [[CrossRef](#)]
29. Wu, Y.; Wen, M.; Navlani-García, M.; Kuwahara, Y.; Mori, K.; Yamashita, H. Palladium nanoparticles supported on titanium doped graphitic carbon nitride for formic acid dehydrogenation. *Chem.-An. Asian J.* **2017**, *12*, 860–867. [[CrossRef](#)] [[PubMed](#)]
30. Navlani-García, M.; Mori, K.; Salinas-Torres, D.; Kuwahara, Y.; Yamashita, H. New approaches toward the hydrogen production from formic acid dehydrogenation over Pd-based heterogeneous catalysts. *Front. Mater.* **2019**, *6*, 44. [[CrossRef](#)]
31. Sun, J.; Qiu, H.; Cao, W.; Fu, H.; Wan, H.; Xu, Z.; Zheng, S. Ultrafine Pd particles embedded in nitrogen-enriched mesoporous carbon for efficient H₂ production from formic acid decomposition. *ACS Sustain. Chem. Eng.* **2019**, *7*, 1963–1972. [[CrossRef](#)]
32. Wang, Z.; Wang, C.; Mao, S.; Gong, Y.; Chen, Y.; Wang, Y. Pd nanoparticles anchored on amino-functionalized hierarchically porous carbon for efficient dehydrogenation of formic acid under ambient conditions. *J. Mater. Chem. A* **2019**, *7*, 25791–25795. [[CrossRef](#)]
33. Wang, X.; Meng, Q.; Gao, L.; Jin, Z.; Ge, J.; Liu, C.; Xing, W. Recent progress in hydrogen production from formic acid decomposition. *Int. J. Hydrog. Energy* **2018**, *43*, 7055–7071. [[CrossRef](#)]
34. Karatas, Y.; Bulut, A.; Yurderi, M.; Ertas, I.E.; Alal, O.; Gulcan, M.; Celebi, M.; Kivrak, H.; Kaya, M.; Zahmakiran, M. PdAu-MnOx nanoparticles supported on amine-functionalized SiO₂ for the room temperature dehydrogenation of formic acid in the absence of additives. *Appl. Catal. B* **2016**, *180*, 586–595. [[CrossRef](#)]
35. Yan, J.M.; Li, S.J.; Yi, S.S.; Wulan, B.R.; Zheng, W.T.; Jiang, Q. Anchoring and upgrading ultrafine NiPd on room-temperature-synthesized bifunctional NH₂-N-rGO toward low-cost and highly efficient catalysts for selective formic acid dehydrogenation. *Adv. Mater.* **2018**, *30*, 1703038. [[CrossRef](#)]
36. Ye, W.; Pei, W.; Zhou, S.; Huang, H.; Li, Q.; Zhao, J.; Lu, R.; Ge, Y.; Zhang, S. Controlling the synthesis of uniform electron-deficient Pd clusters for superior hydrogen production from formic acid. *J. Mater. Chem. A* **2019**, *7*, 10363–10371. [[CrossRef](#)]
37. Luo, Y.X.; Yang, Q.F.; Nie, W.D.; Yao, Q.L.; Zhang, Z.J.; Lu, Z.H. Anchoring IrPdAu nanoparticles on NH₂-SBA-15 for fast hydrogen production from formic acid at room temperature. *ACS Appl. Mater. Interfaces* **2020**, *12*, 8082–8090. [[CrossRef](#)] [[PubMed](#)]
38. Chakravarty, A.; Bhowmik, K.; De, G.; Mukherjee, A. Synthesis of amine functionalized graphite nanosheets and their water-soluble derivative for drug loading and controlled release. *New J. Chem.* **2015**, *39*, 2451–2458. [[CrossRef](#)]
39. Ramanathan, T.; Fisher, F.T.; Ruoff, R.S.; Brinson, L.C. Amino-functionalized carbon nanotubes for binding to polymers and biological systems. *Chem. Mater.* **2005**, *17*, 1290–1295. [[CrossRef](#)]
40. Kitamura, H.; Sekido, M.; Takeuchi, H.; Ohno, M. The method for surface functionalization of single-walled carbon nanotubes with fuming nitric acid. *Carbon* **2011**, *49*, 3851–3856. [[CrossRef](#)]
41. Masuda, S.; Mori, K.; Futamura, Y.; Yamashita, H. PdAg nanoparticles supported on functionalized mesoporous carbon: Promotional effect of surface amine groups in reversible hydrogen delivery/storage mediated by formic acid/CO₂. *ACS Catal.* **2018**, *8*, 2277–2285. [[CrossRef](#)]
42. Luo, Y.X.; Nie, W.; Ding, Y.; Yao, Q.; Feng, G.; Lu, Z.H. Robust hydrogen production from additive-free formic acid via mesoporous silica-confined Pd-ZrO₂ nanoparticles at room temperature. *ACS Appl. Energy Mater.* **2021**, *4*, 4945–4954. [[CrossRef](#)]
43. Yurderi, M.; Bulut, A.; Caner, N.; Celebi, M.; Kaya, M.; Zahmakiran, M. Amine grafted silica supported CrAuPd alloy nanoparticles: Superb heterogeneous catalysts for the room temperature dehydrogenation of formic acid. *Chem. Commun.* **2015**, *51*, 11417–11420. [[CrossRef](#)] [[PubMed](#)]
44. Wang, Q.; Tsumori, N.; Kitta, M.; Xu, Q. Fast dehydrogenation of formic acid over palladium nanoparticles immobilized in nitrogen-doped hierarchically porous carbon. *ACS Catal.* **2018**, *8*, 12041–12045. [[CrossRef](#)]
45. Wang, Q.; Chen, L.; Liu, Z.; Tsumori, N.; Kitta, M.; Xu, Q. Phosphate-mediated immobilization of high-performance AuPd nanoparticles for dehydrogenation of formic acid at room temperature. *Adv. Funct. Mater.* **2019**, 1903341. [[CrossRef](#)]
46. Chaparro-Garnica, J.; Navlani-García, M.; Salinas-Torres, D.; Morallon, E.; Cazorla-Amorós, D. Highly stable N-doped carbon-supported Pd-based catalysts prepared from biomass waste for H₂ production from formic acid. *ACS Sustain. Chem. Eng.* **2020**, *8*, 15030–15043. [[CrossRef](#)]
47. Santos, J.; Megias-Sayago, C.; Ivanova, S.; Centeno, M.; Odriozola, J. Functionalized biochars as supports for Pd/C catalysts for efficient hydrogen production from formic acid. *Appl. Catal. B Environ.* **2021**, *282*, 119615. [[CrossRef](#)]
48. Wang, Z.; Liang, S.; Meng, X.; Mao, S.; Lian, X.; Wang, Y. Ultrasmall PdAu alloy nanoparticles anchored on amine-functionalized hierarchically porous carbon as additive-free catalysts for highly efficient dehydrogenation of formic acid. *Appl. Catal. B Environ.* **2021**, *291*, 120140. [[CrossRef](#)]
49. Yang, S.; Peng, L.; Huang, P.; Wang, X.; Sun, Y.; Cao, C.; Song, W. Nitrogen, phosphorus, and sulfur co-doped hollow carbon shell as superior metal-free catalyst for selective oxidation of aromatic alkanes. *Angew. Chem. Int. Ed.* **2016**, *128*, 4084–4088. [[CrossRef](#)]
50. Bulushev, D.A.; Zacharska, M.; Shlyakhova, E.V.; Chuvilin, A.L.; Guo, Y.; Beloshapkin, S.; Okotrub, A.V.; Bulusheva, L.G. Single isolated Pd²⁺ cations supported on N-doped carbon as active sites for hydrogen production from formic acid decomposition. *ACS Catal.* **2016**, *6*, 681–691. [[CrossRef](#)]

51. Nowicka, E.; Althahban, S.M.; Luo, Y.; Kriegel, R.; Shaw, G.; Morgan, D.J.; He, Q.; Watanabe, M.; Armbrüster, M.; Kiely, C.J.; et al. Highly selective PdZn/ZnO catalysts for the methanol steam reforming reaction. *Catal. Sci. Technol.* **2018**, *8*, 5848–5857. [[CrossRef](#)]
52. Nie, W.; Luo, Y.; Yang, Q.; Feng, G.; Yao, Q.; Lu, Z.H. An amine-functionalized mesoporous silica-supported PdIr catalyst: Boosting room-temperature hydrogen generation from formic acid. *Inorg. Chem. Front.* **2020**, *7*, 709–717. [[CrossRef](#)]
53. Javaid, R.; Kawasaki, S.I.; Ookawara, R.; Sato, K.; Nishioka, M.; Suzuki, A.; Suzuki, T.M. Continuous dehydrogenation of aqueous formic acid under sub-critical conditions by use of hollow tubular reactor coated with thin palladium oxide layer. *J. Chem. Eng. Jpn.* **2013**, *46*, 751–758. [[CrossRef](#)]
54. Yang, F.; Fan, X.; Wang, C.; Yang, W.; Hou, L.; Xu, X.; Feng, A.; Dong, S.; Chen, K.; Wang, Y.; et al. P-doped nanomesh graphene with high-surface-area as an efficient metal-free catalyst for aerobic oxidative coupling of amines. *Carbon* **2017**, *121*, 443–451. [[CrossRef](#)]
55. Yadav, M.; Akita, T.; Tsumori, N.; Xu, Q. Strong Metal-Molecular Support Interaction (SMMSI): Amine-functionalized gold nanoparticles encapsulated in silica nanospheres highly active for catalytic decomposition of formic acid. *J. Mater. Chem.* **2012**, *22*, 12582–12586. [[CrossRef](#)]
56. Zou, L.; Chen, M.; Zhang, Q.; Mao, Q.; Huang, Y.; Liang, Z. Pd/UIO-66/sepiolite: Toward highly efficient dual-supported Pd-based catalyst for dehydrogenation of formic acid at room temperature. *J. Catal.* **2020**, *388*, 66–76. [[CrossRef](#)]
57. Zhang, S.L.; Li, S.J.; Wang, J.Y.; Shang, H.N.; Bai, Y.X.; Liang, J.S. Amine-functionalized carbon nanotubes supported NiAuPd nanoparticles as an efficient in-situ prepared catalyst for formic acid dehydrogenation. *Int. J. Hydrog. Energy* **2021**, *46*, 34727–34736. [[CrossRef](#)]
58. Koh, K.; Jeon, M.; Yoon, C.W.; Asefa, T. Formic acid dehydrogenation over Pd NPs supported on amine-functionalized SBA-15 catalysts: Structure–activity relationships. *J. Mater. Chem. A* **2017**, *5*, 16150–16161. [[CrossRef](#)]
59. Ding, R.D.; Li, Y.L.; Leng, F.; Jia, M.J.; Yu, J.H.; Hao, X.F.; Xu, J.Q. PdAu nanoparticles supported by diamine-containing UiO-66 for formic acid dehydrogenation. *ACS Appl. Nano Mater.* **2021**, *4*, 9790–9798. [[CrossRef](#)]